Accepted, SPIE BiOS - International Biomedical Optics Symposium, February 1998

Incorporation of medical image data in finite element models to track strain in soft tissues

Jeffrey A. Weiss[1,2], Richard D. Rabbitt[2], Anton E. Bowden[2] and Bradley N. Maker[3]

([1]Orthopedic Biomechanics Institute, The Orthopedic Specialty Hospital, SLC, UT 84107)

([2]Department of Bioengineering, University of Utah Salt Lake City, UT 84112-9202)

([3]Livermore Software Technology Corporation, Livermore, CA 94550)

ABSTRACT

A new method has been developed to extract tissue strain from a sequence of two or more medical images. This was achieved by deforming a finite element (FE) model of the tissue under loads derived from the spatial differences between two sets of image data. One image data set deforms with the tissue, while the other remains stationary. The final configuration aligns the two sets of image data. The method accounts for convection of material points, modification of the Lagrangian material properties, and probabilistic features of the sensor. A FE model of the tissue must be constructed and assigned material properties. Image data are assigned to the model tissue such that the reference configuration of the FE model corresponds to one image. The image data is subject to change during the deformation. A nonlinear solution method determines the material configuration that minimizes the difference between the deformed image (deformed template) and the experimentally observed image (target image). In many cases the image data provide powerful constraints which allow estimation of material deformation even in the absence of known loads and/or boundary conditions. The method has been applied to estimate the motion and distribution of strain using MR and CT data.

Keywords: strain measurement, finite element, nonlinear kinematics, anatomical warping

1. INTRODUCTION

The accurate determination of strain in deforming biological tissues is a necessary and important part of many experimental investigations in biomechanics. Previous attempts to estimate nonlinear strains in biological tissues and cells usually employed fiducial markers.[1–8] In some cases, the 3D strain can be estimated directly from changes in the distances between groups of markers making up tetrahedral sets. Inhomogeneous strain fields and physical dimensions of the markers, however, can limit applicability of the method.[2,9,1] The ability to use textural inhomogeneities present in medical images rather than fiduciary markers considerably easier to implement and also would allow for the measurement of soft tissue deformation *in vivo*.

This paper describes a method to estimate stress and strain fields in biological soft tissues that may be applied in the absence of information regarding the tissue constitutive properties or discrete markers to track the deformation. The method makes use of medical image data to provide information about the deforming tissue and thus the strain and stress fields. Accurate stress determinations require a good approximation for the material properties of the tissues under consideration, but even in the absence of stress data, the kinematic data alone provide useful information in both applied and fundamental biomechanical studies ranging from joint mechanics to cell motility.[1,10]

Further author information:
J.A.W.(correspondence): Email: jeff@usi.utah.edu; Telephone: 801-269-4035
R.D.R.: Email: R.Rabbitt@m.cc.utah.edu; Telephone: 801-581-6968
A.E.B.: Email: Anton.Bowden@m.cc.utah.edu; Telephone: 801-581-4549
B.N.M: Email: maker@lstc.com; Telephone: 510-449-2500

2. METHODS

We have developed a method to combine medical image data with a standard solid mechanics analysis approach to allow the estimation of tissue strain fields in the absence of detailed information about boundary conditions and in some cases constitutive information. For the description to follow, it is assumed that a single imaging modality was used to interrogate a fixed 3D volume of space while the material was in a reference configuration (template image) and, at a later time, in a deformed configuration (target image). Standard segmentation and mesh generation methods were used to define a geometrical model of the tissue(s) in the reference configuration. The reference image data were interpolated to the FE model nodes to define a continuous template image intensity field. If CT image data are used, the template image data reflect the initial distribution of material density in the FE model. When the material is deformed, mathematical interrogation of the model generates image data representing a transformed version of the template image field. The mathematical problem is to search through all admissible configurations of the model for the one which minimizes the difference between the transformed template and actual data collected experimentally from the deformed material. There are two formulations of the problem. The first is to assume that the image data provide a hard constraint which must be satisfied exactly. The second is to combine a stochastic model of the imaging sensor (likelihood of the data) with the mechanical model (prior probability), yielding a soft constraint.[11–13] The first case uses Lagrange multipliers[14] or an augmented Lagrangian method[15] and the second uses Bayes theorem or the penalty method.[16] The most effective approach is application-dependent and hence we have used both approaches in the solution of test problems.

2.1. Variational Formulation

The nonlinear solid mechanics problem, subject to the soft (Bayesian) or hard (Lagrange multiplier) constraint imposed by the image data, can be cast in the form of a potential functional. This highly nonlinear functional can be linearized around a known configuration to form the basis for an incremental-iterative solution procedure using a Newton-type method. For an arbitrary domain and boundary conditions, the finite element method is used to discretize the geometry and describe the variations in the unknown field variables over the domain.

Following the standard convention in nonlinear continuum mechanics,[17] material coordinates in the reference configuration are denoted by vector $\mathbf{X}$ while coordinates in the current configuration are $\mathbf{x} = \boldsymbol{\varphi}(\mathbf{X})$. Here $\boldsymbol{\varphi}$ is the deformation mapp. The deformation gradient is defined as $\mathbf{F} := \frac{\partial \boldsymbol{\varphi}}{\partial \mathbf{X}}$. We provide here a brief derivation for the special case of a hyperelastic material, although the method is easily generalized for other material behaviors. In this case the standard mechanical strain-energy density $W(\mathbf{X}, \mathbf{C})$ is augmented with the Gibb's image-energy density $U(\mathbf{X}, \boldsymbol{\varphi}(\mathbf{X}), \mathbf{F}(\mathbf{X}))$. The argument $\mathbf{X}$ denotes dependence of the image data on the initial material configuration and distribution of properties while $\boldsymbol{\varphi}(\mathbf{X})$ and $\mathbf{F}(\mathbf{X})$ denote changes in the image data resulting from convection of the material as well as local deformation. The form of U depends, in part, upon the point-spread function and properties of the imaging hardware. In preliminary results U is taken as a simple Gaussian form, but can be modified to account for other sensor models (empirical or theoretical). The combined optimization problem is to minimize the functional E:

$$E(\boldsymbol{\varphi}) \quad = \quad \int_{\mathcal{B}} W(\mathbf{X}, \mathbf{C}(\boldsymbol{\varphi}(\mathbf{X})))\, dV + \int_{\mathcal{B}} U(\mathbf{X}, \boldsymbol{\varphi}(\mathbf{X}), \mathbf{F}(\mathbf{X}))\, dV, \tag{2.1}$$

where $\mathcal{B}$ denotes integration over the reference configuration. The minimization of the energy functional E will simultaneously minimize internal forces derived from material stresses (W) and deformation-dependent body forces arising from differences between the transformed template image field and the target image data (U, see below). The linearized weak form (Euler-Lagrange equations) is obtained by taking the first and second variations of the energy functional $E(\boldsymbol{\varphi})$ with respect to the deformation to obtain:

$$\begin{aligned} \int_{\boldsymbol{\varphi}(\mathcal{B})} \nabla \mathbf{u} \boldsymbol{\sigma} : \nabla \boldsymbol{\eta} dv + \int_{\boldsymbol{\varphi}(\mathcal{B})} \nabla^s \mathbf{u} : \mathbf{C} \ : \nabla^s \boldsymbol{\eta} dv - \int_{\boldsymbol{\varphi}(\mathcal{B})} \mathbf{u} \cdot \frac{\partial^2 U}{\partial \boldsymbol{\varphi} \partial \boldsymbol{\varphi}} \cdot \boldsymbol{\eta} \frac{dv}{J} \\ = \int_{\boldsymbol{\varphi}(\mathcal{B})} \frac{\partial U}{\partial \boldsymbol{\varphi}} \cdot \boldsymbol{\eta} \frac{dv}{J} - \int_{\boldsymbol{\varphi}(\mathcal{B})} \boldsymbol{\sigma} : \nabla^s \boldsymbol{\eta} dv, \end{aligned} \tag{2.2}$$

Here, $\boldsymbol{\varphi}(\mathcal{B})$ is the deformed configuration, $\mathbf{u}$ and $\boldsymbol{\eta}$ are 1st and 2nd spatial variations, dv denotes integration over the deformed body, $\mathbf{C}$ is the spatial version of the 2nd elasticity tensor (see Marsden and Hughes[17]) and J is the Jacobian. The 4th order elasticity tensor $\mathbf{C}$ provides the constitutive model contribution to the tangent stiffness.[18]

In addition to the standard mechanical terms, the image-based energy density contributes a new term to the tangent stiffness as well as a spatially distributed nonlinear body force. The term $\frac{\partial U}{\partial \boldsymbol{\varphi}}$ provides a deformation-dependent body force, while the term $\frac{\partial^2 U}{\partial \boldsymbol{\varphi} \partial \boldsymbol{\varphi}}$ contributes to the tangent. The body force term provides the force which drives the deformation process. For the case of a single imaging modality with a Gaussian likelihood[13]:

$$U(\mathbf{X}, \boldsymbol{\varphi}(\mathbf{X})) \quad = \quad \frac{\lambda}{2} \left(T(\mathbf{X}, \boldsymbol{\varphi}) - S(\mathbf{X}, \boldsymbol{\varphi}) \right)^2 . \tag{2.3}$$

Here, T and S are the template and target image data fields, respectively.[19] The body force vector is derived from the first derivative of U with respect to the deformation map:

$$\frac{\partial U}{\partial \boldsymbol{\varphi}} \quad = \quad \lambda \left(T(\mathbf{X}, \boldsymbol{\varphi}(\mathbf{X})) - S(\mathbf{X}, \boldsymbol{\varphi}(\mathbf{X})) \right) \left(\frac{\partial T}{\partial \boldsymbol{\varphi}} - \frac{\partial S}{\partial \boldsymbol{\varphi}} \right) . \tag{2.4}$$

In the Bayesian approach, λ is related to the variance in the Gaussian imager model normalized for U to match the same energy density units used for the mechanics W. The Bayesian approach is directly analogous to the penalty method used in mechanics to enforce a constraint in an approximate sense.[16]

2.2. Solution Strategy using the FE Method

We have implemented the image driven algorithm in the nonlinear FE code NIKE3D.[19–21] The unknown variations in shape and displacement over the domain are discretized using the FE shape functions in the standard manner.[18] An iterative Newton procedure is used to obtain the nonlinear solution. Assuming that the solution at a configuration $\boldsymbol{\varphi}^*$ is known, we seek to determine a new configuration $\boldsymbol{\varphi}^* + \mathbf{u}$ that results in a minimization of the energy functional $E(\boldsymbol{\varphi})$. Here $\mathbf{u}$ is a vector of incremental nodal displacements, and the configuration $\boldsymbol{\varphi}^* + \mathbf{u}$ is such that the applied loads/displacements (including image-derived forces) are equilibrated with the internal stresses. The following linearized matrix equations result from the FE discretization:

$$\sum_{i=1}^{N_{\text{nodes}}} \sum_{j=1}^{N_{\text{nodes}}} \left({}^{M}\mathbf{K}(\boldsymbol{\varphi}^*) + {}^{G}\mathbf{K}(\boldsymbol{\varphi}^*) + {}^{I}\mathbf{K}(\boldsymbol{\varphi}^*) \right)_{ij} \mathbf{u} \quad = \quad \sum_{i=1}^{N_{\text{nodes}}} \left({}^{ext}\mathbf{F}(\boldsymbol{\varphi}^*) - {}^{int}\mathbf{F}(\boldsymbol{\varphi}^*) \right)_i . \tag{2.5}$$

The term ${}^{M}\mathbf{K}$ is the material stiffness matrix, while the term ${}^{G}\mathbf{K}$ is the geometric (initial stress) stiffness matrix. These terms both arise in a traditional displacement-based nonlinear analysis. The image-based stiffness, ${}^{I}\mathbf{K}$, is a direct result of the fact that the image-based force changes with configuration. The image-based body forces are applied with other external forces via the vector ${}^{ext}\mathbf{F}$. By solving for $\mathbf{u}$, the configuration at $n+1$ is approximated as $\boldsymbol{\varphi}_{n+1} = \boldsymbol{\varphi}^* + s\mathbf{u}$. Here s is a scalar parameter between 0 and 1 determined by a line search. The determination of an accurate value for $\boldsymbol{\varphi}_{n+1}$ follows by iterative solution of (2.5) using a quasi-Newton strategy.[22]

Equation (2.4) shows that U and the associated driving force both vanish when transformed template image data $T(\mathbf{X}, \boldsymbol{\varphi})$ are equal to target image data $S(\mathbf{X}, \boldsymbol{\varphi})$. The driving body force is also zero if the gradients vanish. The gradient terms determine the direction of the force. Since the appropriate direction can not be determined on a local level without gradient information it is natural that this term vanishes in the absence of a spatial gradient. As a result, inhomogeneous images containing intensity variations and boundaries are most effective in driving the process. The image energy density U also contributes to the tangent stiffness in this implicit formulation.[20]

2.3. Test Problems

The following test problems illustrate the application of the method for strain and stress determination using both simulated and real image data. The first problem simulates the the deformation of a soft rubberlike material by compression between two plates. First, the problem is solved in the "forward" sense using applied displacements to drive the top plate towards the bottom plate. Next, all displacement and contact boundary conditions are removed and the analysis is driven using image data generated from the density distributions that the forward simulation predicted. Excellent agreement between the forward solution and the warping solution was achieved. The second problem utilizes MR image data of the intervertebral disc. In this case the correct strain field in the tissue is unknown and the image data before and after deformation provide a means to estimate it.

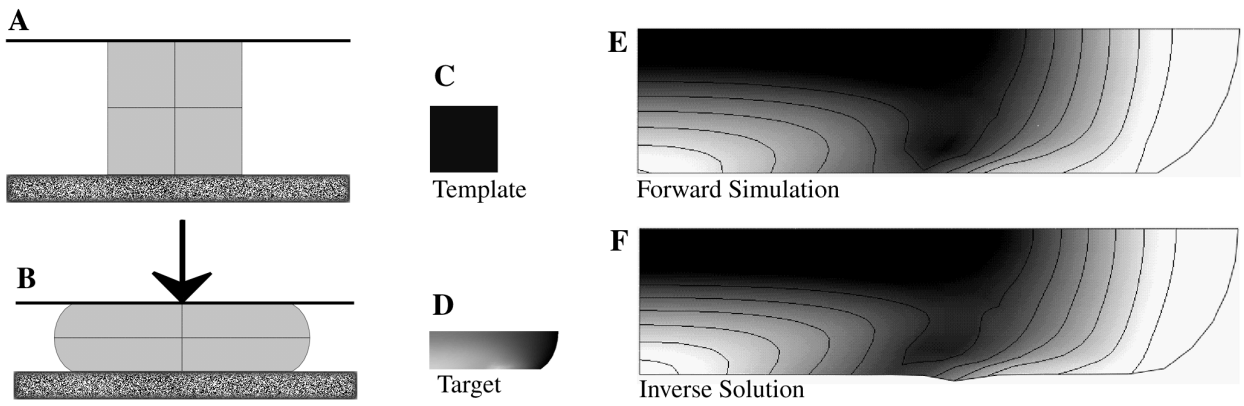

Figure 1. Deformation of a rectangular billet under compression. Panel A is the intial geometry of the billet compressed between two plates. Panel B is the deformed geometry obtained from the forward FE simulation. Panels C and D show the template and target images of the density distribution, used to drive the Warping analysis. Panel E shows the von Mises stress distribution obtained from the forward simulation. Panel F shows the results from the Warping analysis, obtained by removing all applied displacements and contact boundary conditions and using only the pointwise image intensity differences between Panels C and D to drive the analysis.

3. RESULTS

3.1. Stress/Strain Estimation using Simulated CT Data

To test the ability of the warping method to determine stress/strain distributions using "exact" representations for the image data, a traditional FE simulation was performed of a hyperelastic material compressed between two plates (Figure 1A). The material was assumed to be bonded to the plates, and the objective of the analysis was to deform the mesh to 50% axial compression. The sides of the mesh bulge out and eventually contact the plates on the top and bottom (Figure 1B). Contact was modeled with a standard penalty method. This problem is a challenging forward simulation because of the extreme deformation and the contact. The material was assumed to be hyperelastic (compressible Mooney-Rivlin Material model, A=10 MPa, B=5 MPa, bulk modulus=750 MPa) with initially homogeneous density.

Both the forward and inverse solutions were obtained. The forward problem was posed as a standard solid mechanics problem with applied displacements pushing the plates together and contact constraints so that no material would penetrate the infinite plates. For the inverse problem, the applied displacements and contact constraints were removed and the deformation was driven by forces derived from the image-based energy terms in equation (2.1). Images of the density in the reference and deformed configurations obtained from the forward simulation were used as the template and target image data, respectively (Figures 1C and 1D).

The deformed shape of a 1/4 symmetry model and the von Mises stress distribution obtained from the forward simulation are shown in Figure 1E with isocontours indicating lines of constant equivalent stress. To test the warping algorithm, we removed the boundary conditions and the applied loads but added the image-terms to the functional. The problem was then re-run with the two images (1C,D) driving the process. Fig. 1F shows the resulting configuration and isocontours of constant stress for this inverse problem. Notice the excellent correspondence with the forward solution (compare 1E & F). The small error (kink, 1F) at the bottom of the billet could not be eliminated with the image-driven analysis. This is due to the use of the penalty method where the parameter λ was increased during the simulation using a load curve. The maximum value of λ that can be used in the computation is controlled by numerical precision. Since the simulated CT data was perfect in this test case, λ should be allowed to approach infinity, in theory. This is not computationally feasible. An augmented Lagrangian or Lagrange multiplier method, in combination with a more refined mesh along the bottom edge of the domain, should alleviate this shortcoming.

Figure 2 illustrates a sequence of the deforming mesh for both the forward and inverse problems. The forward problem (top panels) proceeds by compression of the material as specified by the applied displacements and contact

conditions. During the compression, the side of the original mesh eventually contacts the compressing plate and the material continues to bulge out between the plates. In the case of the inverse image-driven problem (bottom panels), the deformation proceeds along a very different path as specified by the pointwise difference in template and study intensities and their gradients. However, the end state is almost identical to that obtained from the forward solution. The actual path of deformation taken by the forward problem can only be reproduced in the inverse problem if a sufficient number of intermediate images are employed in the deformation process.

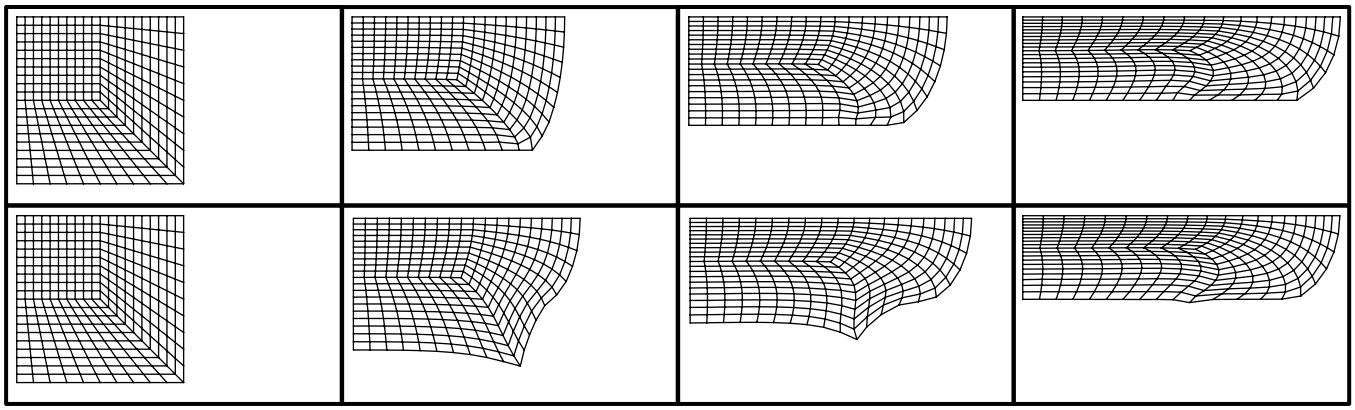

Figure 2. Sequence of images from the forward (top panels) and inverse (bottom panels) solution of the compression of a beam between two plates. Only the bottom right portion of the beam was modeled because of symmetry. The mesh of the forward solution is gradually compressed and eventually the side of the mesh contacts the plate as the deformation progresses to 50% axial compression. The inverse solution follows an entirely different path as dictated by the image data and its gradients, but eventually reaches the same final configuration.

3.2. Intervertebral disc strain extracted using MR images

We also have tested the FE implementation by using MR data to track strain in a spinal disc.[23] The human intervertebral disc is a complex combination of materials, including collagen, water, and a proteoglycan matrix. Material characterization and strain measurement are extremely difficult for the disc. Using a nonmagnetic compression frame and a MRI scanner, MR images of a L2-L3 motion segment were obtained before and after application of a 250 lb compressive load (data supplied by Chiu et al.,[24] Figs. 3A, B). The image in the reference configuration was used to generate geometrical models of the disc and bone. Pixel intensities from the reference image were assigned to the model to define the template image field. Image data were filtered at the spatial Nyquist frequency of the FE mesh to avoid aliasing. Representative hypoelastic material properties were estimated from the literature[25] as described by Bowden et al. (1997).[23] Differences between the template and target images defined the only input "force" driving the deformation of the disc and bone. As the Warping code registered the two images, strains developed in the spinal disc. The difference images before and after deformation illustrate the excellent registration that was achieved (Figs. 3C, D). Results show changes in volume of up to 15% and compressive strains as high as 20% within the disc[23] (Figs. 3E, F). The computed deformation was insensitive to changes in the elastic moduli due to the path independent nature of the elastic response. This insensitivity does not hold for Poisson's ratio owing to the interplay between the volume ratio and strain. Due to lack of volumetric information in two-dimensional problems the computed strain field is sensitive to the compressibility of the material. The best results for 2D data are therefore obtained when the model material properties match the actual tissue.[23]

4. DISCUSSION

The paper presented a finite-element based method that combines 2D or 3D image-based data with nonlinear continuum mechanics to track the motion and deformation of materials. This was achieved using a nonlinear variational approach which simultaneously minimizes energy functional associated with the image data and with the mechanical model. The derivation was presented for hyperelastic materials, but the approach is not in any way limited to this material type. When used with medical image data, it provides a means to estimate tissue strains *in vivo*.

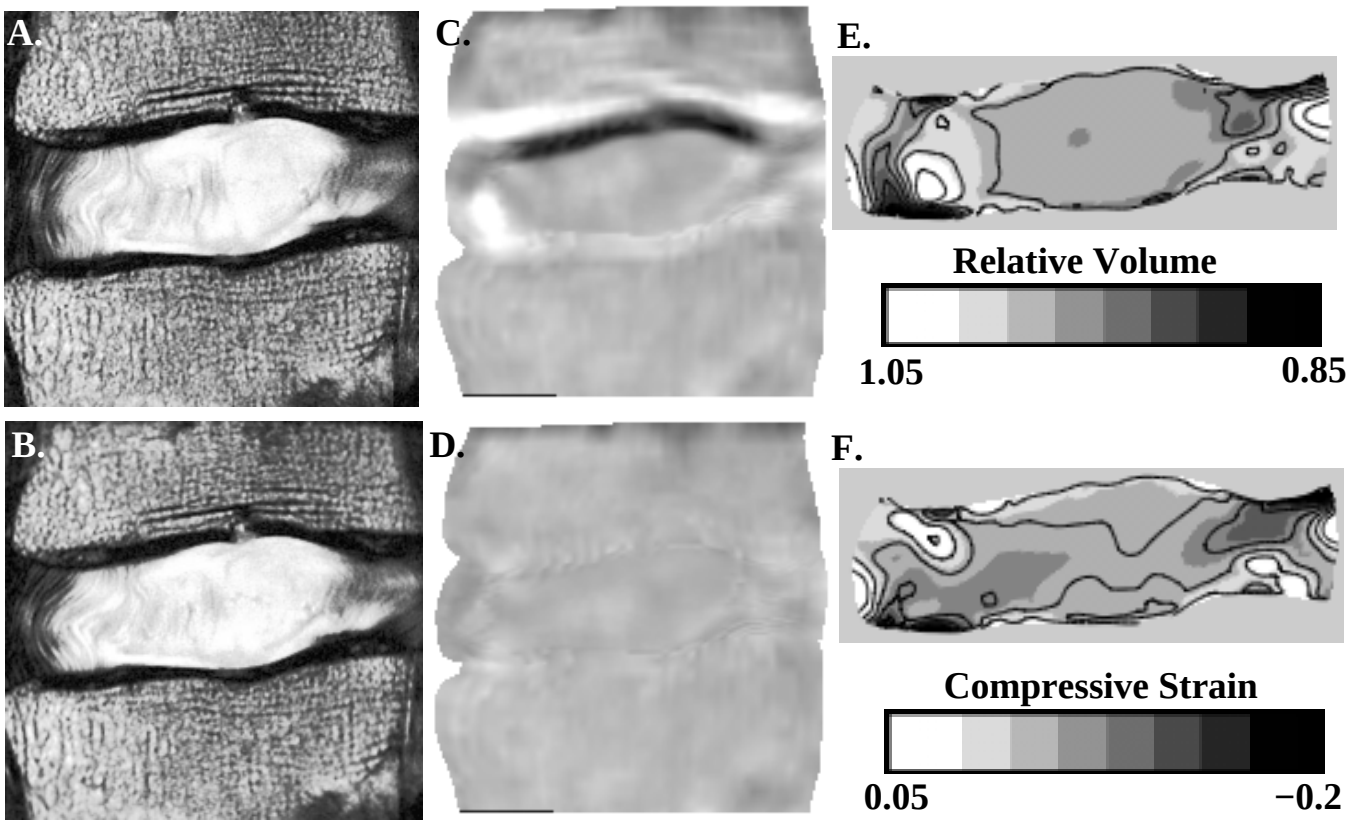

Figure 3. Intervertebral disc strain. Images on the left show the template (A) and target (B) images. Center panels show the difference images prior to deformation (C) and after deformation (D). The resulting volume ratio (E) and and compressive strain (F) are shown on the right with isocontours.

The implementation must be modified to accommodate nonconservative systems which exhibit path dependent behavior. The time sequence of images shown in figure 2 clearly illustrate that the path determined by the image-driven deformation is distinct from the actual path, even though the final configuration is approximately the same. The difference in path is due to the fact that the deformation is driven only by the initial and final images. Intermediate images are not used in this example and hence the algorithm has no information concerning the path other than that built into the a priori mechanical model. Since the applied boundary conditions were neglected in the image-based result, the resulting path is different. For hyperelastic materials this difference does not influence the final stress state and therefore is not a concern. For general materials the path is crucial and must be accurately reproduced. One way to achieve this is to use a time sequence of images that are spaced so that the path is resolved sufficiently.

The specific content of the images can affect the ability of the method to reproduce a defined deformation field. Sharp boundaries, such as present in Example 1, provide strong gradient information that controls the direction of the image-derived body forces as defined in equation (2.4). This can result in better end-registration, but also causes severe nonlinearities for the incremental-iterative solution process. We have used image blurring to circumvent this problem. By starting with blurred versions of the template and target images and gradually sharpening them as the analysis proceeds, excellent results are often obtained. The opposite problem can occur when the image consists of diffuse gradient information. In this case local minima can complicate the solution process. Again image blurring or other ad-hoc processing techniques can be used in this case.

In summary, a method for combining medical image data with nonlinear continuum mechanics has been developed and used to determine strain distributions in the absence of detailed information about applied loads or boundary

conditions. The method appears to hold promise for in vivo strain determination using image data obtained from noninvasive imaging modalities such as MR. Future work will assess the sensitivity and accuracy of the method for materials undergoing well-defined deformations.

ACKNOWLEDGEMENTS

Partial support for this work was provided by the Whitaker Foundation; The NIMH, NSF and NASA under the Human Brain Project, # RO1 MH/DA52158; The University of Utah Research Foundation; The University of Utah Center for High Performance Computing. MRI images of the intervertebral disc were provided by Elaine J. Chiu, Sharmila Majumdar, Neil A. Duncan and Jeffrey C. Lotz.

REFERENCES

1. S. I. Simon and G. W. Schmid-Schonbein, "Cytoplasmic strains and strain rates in motile polymorphonuclear leukocytes," *Biophysical J.* **58**, pp. 319–332, 1990.
2. A. D. McCulloch, B. H. Smaill, and P. J. Hunter, "Regional left ventricular epicardial deformation in the passive dog heart," *Circ Res* **64**, pp. 721–733, 1989.
3. J. W. Holmes, Y. Takayama, I. LeGrice, and J. W. Covell, "Depressed regional deformation near anterior papillary muscle," *Am J Physiol* **269(1 Pt 2)**, pp. H262–70, 1995.
4. Z. Jia and S. P. Shah, "Two-dimensional electronic-speckle-pattern interferometry and concrete-fracture processes," *Exp Mech* **34(3)**, pp. 262–70, 1994.
5. E. H. Jordan, S. C. U. Ochi, D. Pease, and J. I. Budnick, "Microradiographic strain measurement using markers," *Exp Mech* **34(2)**, pp. 155–165, 1994.
6. J. O. Hjortdal and P. K. Jensen, "In vitro measurement of corneal strain, thickness, and curvature using digital image processing," *Acta Ophthalmol Scand* **73(1)**, pp. 5–11, 1995.
7. D. J. Wissuchek, T. J. Mackin, M. DeGraef, G. E. Lucas, and A. G. Evans, "Simple method for measuring surface strains around cracks," *Exp Mech* **36(2)**, pp. 173–9, 1996.
8. H. van Bavel, M. R. Drost, J. D. L. Wielders, J. M. Huyghe, A. Huson, and J. D. Janssen, "Strain distribution on rat medial gastrocnemius (mg) during passive stretch)," *J Biomech* **29(8)**, pp. 1069–74, 1996.
9. L. K. Waldman, Y. C. Fung, and J. W. Covell, "Transmural myocardial deformation in the canine left ventricle: Normal in vivo three-dimensional finite strains," *Circ Res* **57**, pp. 152–163, 1985.
10. R. Skalak, C. Dong, and C. Zhu, "Passive deformations and active motions of leukocytes," *J. Biomech. Eng.* **112**, pp. 295–302, 1990.
11. M. I. Miller, G. E. Christensen, Y. Amit, and U. Grenander, "Mathematical textbook of deformable neuroanatomies," *Proceedings of the National Academy of Science* **90**, pp. 144–48, dec 1993.
12. U. Grenander, *Lectures in Pattern Theory I, II, and III: Pattern Analysis, Pattern Synthesis and Regular Structures*, Springer-Verlag, 1976.
13. G. E. Christensen, R. D. Rabbitt, and M. I. Miller, "Deformable templates using large deformation kinematics," *IEEE Trans on Image Processing* **5**(10), pp. 1435–1447, 1996.
14. J. N. Reddy, *Energy and variational methods in applied mechanics*, John Wiley, 1984.
15. J. C. Simo and R. L. Taylor, "Quasi-incompressible finite elasticity in principal stretches: Continuum basis and numerical algorithms," *Comp Meth Appl Mech Engng* **85**, pp. 273–310, 1991.
16. A. M. Maniatty and N. J. Zabaras, "Investigation of regularization parameters and error estimating in inverse elasticity problems," *Int J. for Numerical Meth. in Eng.* **37**, pp. 1039–1052, 1994.
17. J. E. Marsden and T. J. R. Hughes, *Mathematical Foundations of Elasticity*, Dover, Minneola, New York, 1994.
18. K.-J. Bathe, *Finite Element Procedures*, Prentice-Hall, Englewood Cliffs, New Jersey, 1996.
19. R. D. Rabbitt, J. A. Weiss, G. E. Christensen, and M. I. Miller, "Mapping of hyperelastic deformable templates," in *Proceedings of the International Soc. for Optical Engineering*, vol. 252, pp. 252–265, SPIE, 1995.
20. J. Weiss, R. D. Rabbitt, and B. N. Maker, "Use of image data to regularize ill-posed problems in solid mechancis," *In Review, Int. J. Numer. Methods Engng.* , 1996.

21. B. N. Maker, R. M. Ferencz, and J. Hallquist, "Nike3d: A nonlinear, implicit, three-dimensional finite element code for solid and structural mechanics," *Lawrence Livermore National Laboratory Technical Report* **UCRL-MA**(105268 Rev. 1), 1995.
22. H. Matthies and G. Strang, "The solution of nonlinear finite element equations," *Int J Numer Methods Eng* **14**, pp. 1613–1626, 1979.
23. A. Bowden, R. Rabbitt, J. Weiss, and B. Maker, "Use of medical image data to compute strain fields in biological tissue," *Proc ASME Bioengineering Conference* **BED-35**, pp. 191–192, 1997.
24. E. Chiu, J. Lotz, and S. Majumdar, "High resolution magnetic resonance imaging of the human intervertebral disc with compression," *Trans. 41st Orthopaedic Research Society* **20(2)**, p. 292, 1995.
25. Y. Liu, G. Ray, and C. Hirsch, "The resistance of the lumbar spine to direct shear," *Orthopadic Clinics of North America* **16(1)**, pp. 33–47, 1975.